CERN Summer Student Report
August 2024
Thiago.de.andrade.rangel.monteiro@cern.ch

Performance of CO_2 based mixture in CMS Improved Resistive Plate Chambers in HL-LHC

Thiago de Andrade Rangel Monteiro[1]
CERN, Geneva, Switzerland
Supervisors: Mehar Ali Shah[2], João Pinheiro [3]

[1] Brazilian Center for Physics Research, Rio de Janeiro, Brazil
[2] Universidad Iberoamericana, Mexico City, Mexico
[3] Rio de Janeiro State University, Rio de Janeiro, Brazil

Keywords: LHC, CMS, iRPC, muon detector, Gaseous detectors, Resistive-plate Chambers, eco-friendly gas mixtures

Summary

The Resistive Plate Chamber (RPC) is a muon detector based in gas ionization known by its timing resolution. There are 1,056 RPCs placed in the Compact Muon Solenoid (CMS) experiment at the Large Hadron Collider (LHC) taking data since Run I with stable performance. In the view of Phase-II Upgrade of LHC (High-Luminosity LHC), 72 new generation of RPCs, so called improved RPCs (iRPC) will be placed in the forward region of CMS. The RPCs utilizes a gas mixture composed of 95.2% $C_2H_2F_4$, 4.5% iC_4H_{10} and 0.3% SF_6. New regulations from Europe Union (EU) and CERN are imposing restrictions in the usage of F-gases, since most of CERN emission is due to experiments usage. $C_2H_2F_4$ is a potent greenhouse gas, with a global warming potential (GWP) of 1430, so new strategies are being implemented in order to reduce or ban its use. A promising option, described in the present report, is the reduction of the $C_2H_2F_4$ in the CMS-RPC gas mixture's GWP by substituting this gas with some amount of CO_2. The study is conducted at CERN's Gamma Irradiation Facility and explores the performance of a 1.4 mm gap iRPC prototype using three different CO2-based mixtures (30% and 40% CO_2 varying SF_6 from 0.5 to 1.0%) under conditions similar to the ones expected in the High-Luminosity (HL) LHC phase.

Contents

List of Figures

List of Tables

1 Introduction

The CMS experiment, located at the LHC on the border between France and Switzerland, is a versatile detector designed to study both proton and heavy-ion collisions. Renowned for its muon detection capabilities, CMS played a crucial role, alongside ATLAS, in the groundbreaking discovery of the Higgs boson in 2012 [8][9], a key achievement in validating and consolidating the Standard Model of particle physics.

Despite the significant accomplishments of the CMS Collaboration, the quest for new physics, particularly in the realm of "Beyond the Standard Model" theories, remains an immense challenge. To push the boundaries of discovery, a major upgrade to the LHC, known as the High-Luminosity LHC (HL-LHC) or Phase-2, has been proposed.

The HL-LHC is an upgrade scheduled to occur after the third Long Shutdown (LS3) of LHC, aimed at increasing the LHC's integrated luminosity by a factor from 5 to 7.5 [10][11] compared to current levels, resulting in a substantially higher rate of collisions. This boost in luminosity is crucial for gathering more comprehensive data, enabling the observation of rare processes and the potential discovery of new particles, such as heavy gauge bosons and phenomena beyond the Standard Model.

However, the increase in luminosity also brings a significant rise in the number of simultaneous collisions per event, known as pile-up, which will increase to approximately 100 proton-proton interactions for every bunch crossing, occurring every 25 ns, yielding billions of secondary particles each second. This increased pile-up poses a challenge for data analysis, as overlapping collisions make it more difficult to accurately reconstruct individual events and particle decays.

Moreover, the heightened luminosity will lead to an increase in radiation levels within the detector environment. Not only the performance of the detectors must be evaluated in that level of radiation, but also over time this increased radiation can degrade the performance of detector components, potentially leading to failures or the need for more frequent maintenance and replacements. As the muon systems are a critical part of CMS, they must be rigorously tested for resilience to these elevated radiation levels to ensure their long-term functionality and reliability in registering muons and differentiating between multiple muons passing through the detector.

Given these challenges, a thorough evaluation of the CMS detectors' adaptability is essential, particularly in their ability to withstand the combined effects of high luminosity, increased pile-up, and elevated radiation. As a result, an extensive research and development program has been initiated to ensure that the CMS muon systems continue to operate efficiently under the demanding conditions imposed by the HL-LHC. These efforts are critical for CMS to maintain its leading role in exploring high-energy physics and in the ongoing search for new physics beyond the Standard Model.

In addition to these technical challenges, CERN and the CMS experiment are also addressing environmental concerns associated with the use of gaseous detectors. Some traditional detector gases (as $C_2H_2F_4$) can have a significant impact on the environment due to their high global warming potential. To mitigate this, CMS is actively researching alternative gases that could reduce the environmental footprint of the experiment. By focusing on more sustainable options, CMS aims to minimize the ecological impact of its operations while continuing to contribute to our understanding of the universe.

CERN aims to achieve zero F-gas emissions by 2050 and reduce emissions by 28% by the end of Run III, compared to 2018 levels [12]. These goals align with the European Union's targets of reducing GHG emissions by 55% by 2030 and achieving net-zero emissions by 2050 [13].

2 CMS Resistive Plate Chambers

The CMS experiment consists of four principal subdetectors: the inner tracker, the electromagnetic calorimeter, the hadronic calorimeter, and the muon chambers. Among these, the muon chambers play a crucial role in detecting and measuring muons, which are essential for detector calibration and many key analyses, particularly those involving precision measurements and searches for new physics.

Muons are ideal particles for precise identification and measurement. In the CMS detector, the muon chambers form the outermost layer, ensuring that, in most cases, only muons generate signals in these detectors. This is due to their relatively long lifetime and weak interaction with matter, allowing them to traverse significant distances through the detector without interacting with other subdetectors. Consequently, they can be detected distinctly in the muon chambers. Additionally, muons are easily distinguishable from the large hadronic background, as they are often the only particles to leave a signal in the muon detectors.

The CMS experiment has developed several complementary subdetectors for muon identification, enabling precise measurements of their charge and momentum across a wide range of pseudorapidity, even at the trigger level. However, the CMS currently lacks sufficient coverage in the high pseudorapidity (η) region, where background noise is highest and the magnetic field integral is relatively low. This makes muon triggering, identification, and measurement in this region particularly challenging. To address these challenges, different types of detectors have been implemented in CMS, as illustrated in Figure 1.

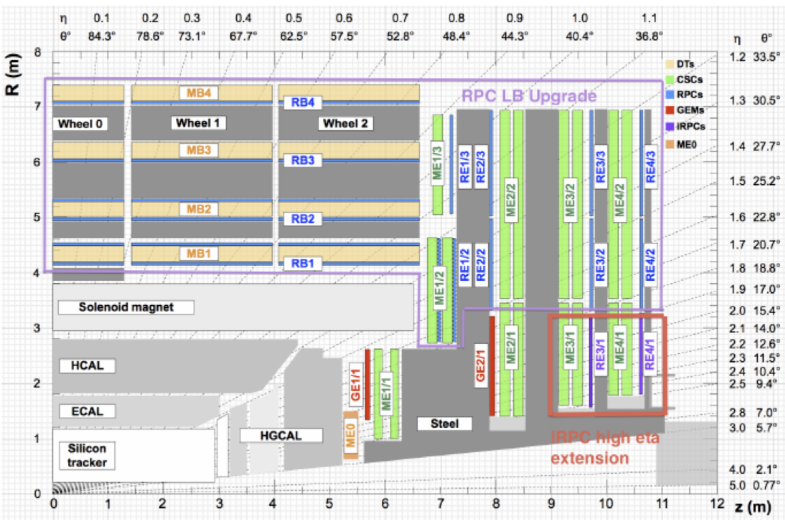

Figure 1: A quadrant of the CMS experiment. The red box indicates the region where iRPCs will be placed by the iRPCs to extend the muon coverage.

The muon detection system in the CMS consists primarily of three types of detectors: Resistive Plate Chambers (RPCs), Cathode Strip Chambers (CSCs), and Drift Tubes (DTs). The CSCs are located in the endcaps of the CMS detector, where they are particularly effective at precisely determining the position of muons in these challenging environments. By recording the charge distribution on the cathode strips as a muon passes through, the CSCs provide accurate measurements of the muon's trajectory.

The Drift Tubes (DTs), located in the barrel region of the CMS detector, are designed to measure the position of muons with high accuracy by recording the time it takes for ionization electrons to drift to the anode wires. The DTs are particularly effective in areas of the detector where the magnetic field is relatively uniform, providing detailed spatial information that enables precise reconstruction of muon tracks within the barrel region.

As shown in Figure 1, the muon system in the endcap incorporates a new detector technology: the Gas Electron Multipliers (GEMs). GEM detectors consist of thin metallic foils with microscopic holes, across which electric fields are applied. As ionizing particles traverse these foils, they generate and amplify electrons, enabling GEMs to achieve a good spatial resolution and high-rate capabilities, making them suited for high-radiation environments.

Designed to cover the pseudorapidity ranges $1.6 < |\eta| < 2.4$ for GEMs and $2 < |\eta| < 2.8$ for ME0, these detectors significantly enhance the reliability and precision of muon detection. Some of the first-generation GEM detectors (GE1/1) were installed during Long Shutdown 2 (LS2) and are currently being integrated into the CMS data acquisition system. The installation of the second generation (GE2/1) is ongoing in phases during the Year-End Technical Stops (YETS), with completion expected after LS3.

Scheduled for installation during LS3 alongside the new HGCAL, the ME0 are six layers GEMs chambers that will markedly improve muon detection capabilities in the forward regions. Together with the other GEMs, these new chambers will enhance coverage and precision in muon tracking, playing an essential role in ensuring the optimal performance of the CMS detector throughout the HL-LHC era.

And finally the core of muon detection, the Resistive Plate Chambers (RPCs) are gaseous detectors renowned for their excellent time resolution. Positioned in both the barrel and endcap regions of the CMS detector, RPCs are critical for triggering muon detection, delivering precise timing information essential for distinguishing between closely spaced collision events.

The CMS detector includes a total of 1,056 RPC chambers, with 480 situated in the barrel and the remaining 576 positioned in the endcap region. These chambers are systematically arranged into four stations, labeled RB1 to RB4 in the barrel zone, and RE1 to RE4 in the endcap domain.

The innermost stations in the barrel, RB1 and RB2, are equipped with two RPC chambers each, while all other RPC stations contain a single RPC chamber. In the endcap there are 36 chambers per ring, distributed in rings 2 and 3 for all endcap stations. The complete RPC configuration within the CMS detector is illustrated in Figure 2.

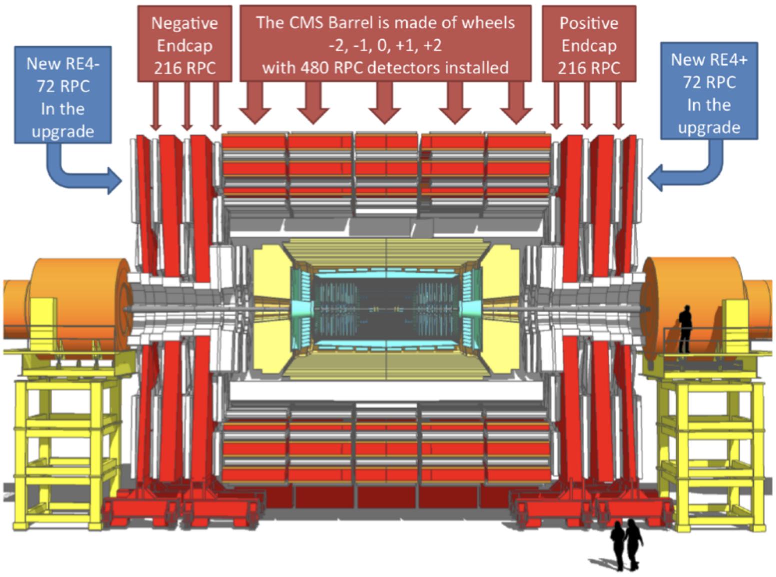

Figure 2: RPC chamber distribution in the CMS experiment [1]

The exitings RPCs are double-gap chambers that operate in avalanche mode under a electric field around 9.8 kV. The standard gas mixture is composed of 95.2 % of $C_2H_2F_4$, 4.5 % of iC_4H_{10}, and 0.3 % of SF_6. The $C_2H_2F_4$ acts as the primary component, responsible for the initial ionization that enables electron avalanches. Under the influence of the strong electric field, the free electrons are accelerated and collide with additional $C_2H_2F_4$ molecules, causing further ionization and creating an electron avalanche, as depicted in Figure 3.

The other gases, such as iC_4H_{10}, function as quenching agents, regulating the electron amplification and preventing excessive ionization that could potentially damage the detector. In addition, SF_6 plays a crucial role in suppressing continuous discharges within the chamber, ensuring stable and reliable operation [14].

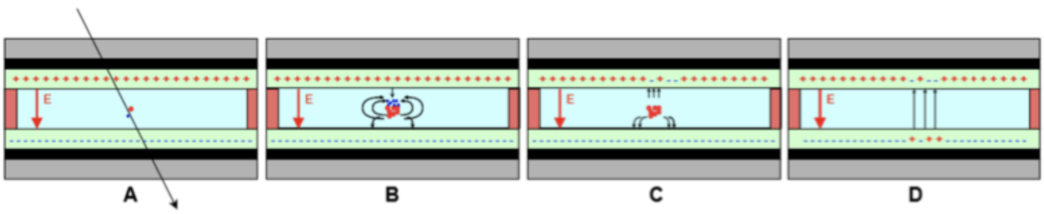

Figure 3: View of an iRPC operating in avalanche mode. (A) The passage of a particle ionizes molecules in the gas. (B) The size of the avalanche influences the local field. (C) The electrons reach the anode. (D) The ions reach the cathode. The charge is induced [2].

When a muon passes through the gas mixture, it ionizes the molecules, creating free electrons. The electric field accelerates the electrons ionizating other molecules, creating an avalanche. The avalanche then induces a current in the readout strips, placed between the gas gaps, which is then sent to the detector electronics. In the standard RPCs the signal position is determined by the location of the strip that collects the charge. The position resolution in a standard RPC depends on the width of the strips and the detector's segmentation, with the signal being read out from only one side of each strip, giving a spatial resolution in η direction of approximately 20-28 cm (segmentation) and in ϕ of 0.8-1.9 cm (strips width).

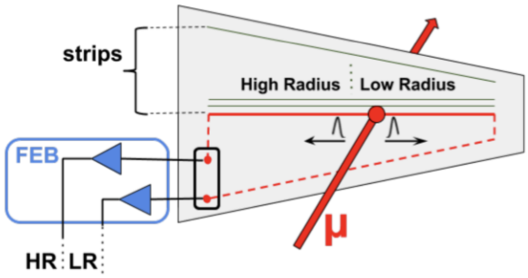

Figure 4: View of the working principle of an iRPC chamber with the TDoA method for calculating the position of the signal on the board [3].

The double-gap design of the RPCs further enhances their efficiency by providing two layers where ionization and the subsequent avalanche process can occur, thereby increasing the likelihood of detecting passing particles. This design makes RPCs particularly effective for triggering and timing applications within the CMS muon system, where precise timing is crucial for accurately reconstructing particle trajectories and distinguishing between events in different bunch crossings.

The RPCs are constructed with High-Pressure Laminate (HPL) for the electrodes, known for its high bulk resistivity, see Table 1. This characteristic is essential for minimizing leakage current and maximizing the detector's efficiency.

The HPL in the RPC detectors has a thickness of 2 mm, which provides an intrinsic timing resolution of approximately 1.5 ns for muon detection. Each double-gap chamber is designed to operate at voltages up to 9.8 kV, ensuring effective detection and rapid response to events. The schematic layout of the detector, including the electrode arrangement and key components, is shown in Figure 5.

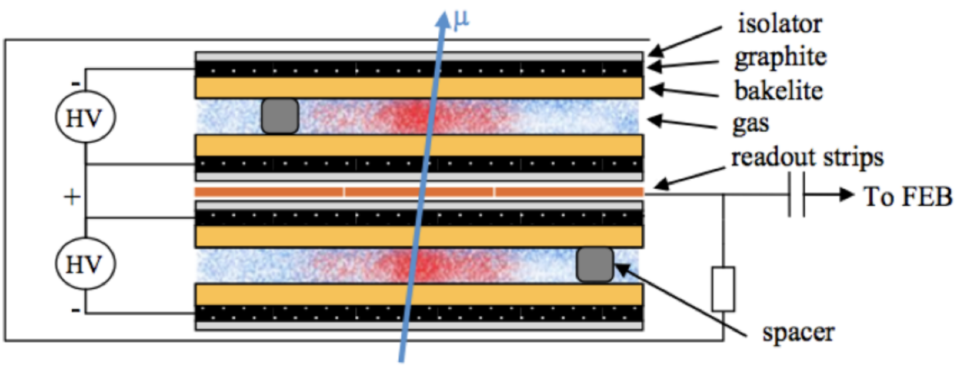

Figure 5: Schematic view of the double gap RPCs detect muon in CMS [3].

For the HL-LHC, the existing detectors will pass through a electronics upgrade. The electronics associated with the RPCs will be upgraded to manage the increased data flow and ensure faster signal processing. This enhancement will enable the detectors to improve their high timing resolution and maintain efficiency despite the dramatically higher collision rates. With the new electronics, the timing resolution will be refined from 25 ns nowadays to 1.5 ns, achieving the intrinsic timing resolution of the chambers.

In the high η region, a new generation of RPCs will be installed, aiming to increase the coverage of the existing system (from 1.9 to 2.4) and play the role of muon reconstruction and triggering in a region never exploited before for RPCs. The background gamma rate expected in this region is around 600-700 Hz/cm^2. The improved Resistive Plate Chambers (iRPCs) represent a significant advancement over the existing RPCs in the CMS experiment. These upgrades focus on enhancing background hit rejection, improving the identification and reconstruction of slowly moving, heavy, stable charged particles, and achieving superior spatial resolution, with an accuracy of a few centimeters along the strip direction, thanks to the readout from both strip ends. The spatial resolution of the iRPCs are of 0.3-0.6 cm in ϕ direction and 1.5 cm in η direction.

To realize these improvements, new chambers are in mass production phase in order to include two 1.4 mm HPL electrodes per gap, with a gas gap of matching thickness between them. Additionally, a new Front-End Board (FEB) has been designed to read out both ends of the pickup strips on a Printed Circuit Board (PCB) panel situated between these gaps. The FEB charge threshold is up to 30-40 fC (instead of 150 fC of existing system).

The gaps and PCB strips are shielded from electromagnetic interference by a copper layer, and the entire assembly is encased within an aluminum honeycomb framework to ensure structural integrity and protection as shown in the Figure 6.

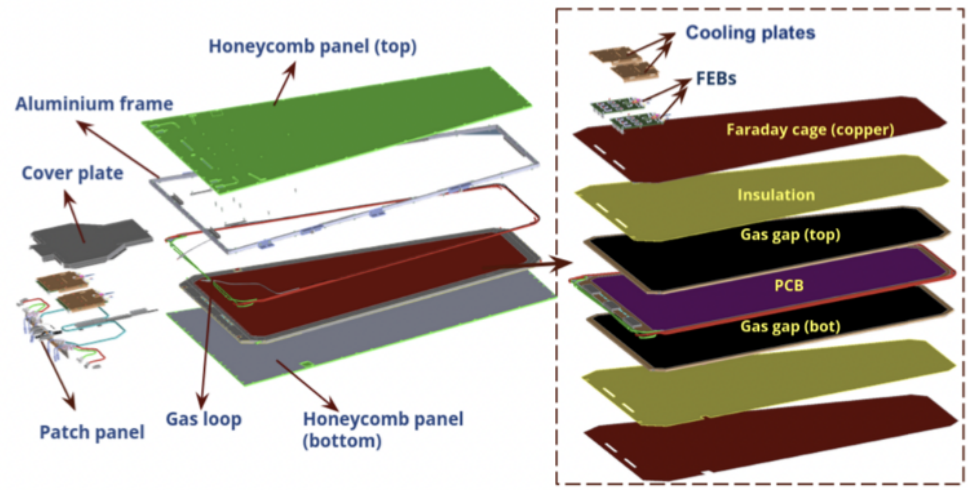

Figure 6: Schematic layout of the iRPC chamber [4].

Each iRPC comprises a pair of HPL panels coated with a layer of graphite, with a spacer inserted between the panels to define the gas gap size. The graphite coating on the panels is subjected to a high voltage to create the required electric field within the gap.

The iRPCs will continue to operate using the avalanche method, similar to the original RPCs, while enhancing the timing resolution necessary for the CMS muon system up to 500 ps, thanks to thinner gas gaps, also enhacing the rate capability of the detector. These improvements are especially crucial for the high-luminosity environment of the HL-LHC.

In summary, Table 1 highlights the principal differences between the RPCs and the iRPCs. With these advancements, the muon detection capabilities of the CMS experiment will be significantly enhanced, especially in the demanding environment of the HL-LHC. The iRPCs provide improved spatial resolution, faster intrinsic time resolution, and enhanced charge sensitivity, which are essential for accurately reconstructing muon trajectories and distinguishing between closely spaced events.

	iRPC	**RPC**
High Pressure Laminate Thickness	1.4 mm	2 mm
Number of Gas Gaps	2	2
Gas Gap Thickness	1.4 mm	2 mm
Resistivity (Ω·cm)	$0.9 - 3 \times 10^{10}$	$1 - 6 \times 10^{10}$
Charge Threshold	< 50 fC	150 fC
Space Resolution (η)	1.5 cm	20-28 cm
Space Resolution (ϕ)	0.3-0.6 cm	0.8-1.9 cm
Intrinsic Time Resolution	0.5 ns	1.5 ns

Table 1: Comparison of iRPC and RPC characteristics [4].

3 The Gaseous Study for the iRPCs

The choice of an alternative gas mixture is pivotal in determining the iRPCs' performance, influencing factors such as ionization efficiency, signal amplification, and timing resolution. The primary aim is to find a gas mixture that maximizes muon detection efficiency while minimizing spurious signals that could complicate data analysis. Additionally, the selected gas mixture must be stable under the high-radiation conditions expected at the HL-LHC to ensure consistent long-term performance.

Environmental sustainability is also a growing concern. Many traditional detector gases have a high global warming potential (GWP), such as $C_2H_2F_4$ and SF_6. Consequently, part of the ongoing research involves finding alternative gases or mixtures with a lower GWP, reducing the environmental impact of the iRPCs while maintaining or even enhancing their performance.

Extensive testing and simulations are being conducted to evaluate various gas mixtures under realistic operating conditions. The results of these studies will be crucial in selecting the gas mixture for the upgraded iRPCs, ensuring they achieve high performance and environmental responsibility. These efforts are essential for the effective operation of the iRPCs in the CMS experiment.

Currently, the standard gas mixture used by the CMS RPC system includes tetrafluoroethane ($\mathrm{C_2H_2F_4}$), which is responsible for the avalanche; isobutane ($\mathrm{iC_4H_{10}}$), which controls the avalanche; and sulfur hexafluoride ($\mathrm{SF_6}$), which prevents continuous discharges within the chamber. This combination has been optimized to balance efficient muon detection and stable operation.

The most promising gas to replace the $C_2H_2F_4$, at least for a the moment, is the tetrafluoropropene ($C_3H_2F_4$ or simply HFO) [15], some eco-friendly gas mixtures that have been testing remove all the Freon and replace it by a combination of HFO and CO_2. These mixtures aim to significantly lower GWP while maintaining the high efficiency and stability required for the operation of the RPCs.

Although HFO/CO_2-based mixtures show promising results in terms of reducing environmental impact, their long-term performance and compatibility with the stringent requirements of high-energy physics experiments remain under investigation. While these mixtures provide a long-term alternative to traditional gases like $C_2H_2F_4$ and SF_6, further research is essential to fully assess their effectiveness and reliability.

On the other hand, some urgent decisions should be taken in the present and mid-term solutions are being addressed. One strategy is to replace partially $C_2H_2F_4$ by certain amount of CO_2, an inert priceless gas. ATLAS experiment has being injecting 30% of CO_2 in the RPCs since July 2023 and, despite higher current, no performance degradation has been observed so far [16].

These mixtures, analyzed in this study, are summarized in Table 2. They were selected to assess how different amounts of CO_2 (inert and cheap gas) and SF_6 (compensates the high streamer probability induced by the addition of CO_2) affect detector efficiency, given the GWP of the mixture.

Component	**Standard Mixture**	**30% CO_2 + 1% SF_6**	**30% CO_2 + 0.5% SF_6**	**40% CO_2 + 1% SF_6**
Freon ($C_2H_2F_4$)	95.2%	64%	64.5%	54%
Isobutane (iC_4H_{10})	4.5%	5%	5%	5%
CO_2	0%	30%	30%	40%
SF_6	0.3%	1%	0.5%	1%
GWP	1486	1529	1337	1353

Table 2: Comparison of gas mixtures used in the CMS iRPC system with their Global Warming Potential (GWP) [7].

4 Gamma Irradiation Facility

To evaluate various gas mixtures for the detectors, the CMS experiment utilizes the Gamma Irradiation Facility (GIF++), located at the Prevessin Site in the North Area of the SPS at CERN. GIF++ combines a ^{137}Cs gamma source with two sets of adjustable filters to control radiation intensity, along with a high-energy muon beam (100-150 GeV/c) from the SPS H4 secondary beamline in EHN1. The facility's layout is illustrated in Figure 5.

GIF++ is specifically designed to replicate the extreme conditions anticipated during Phase II of the LHC, ensuring both the safety of personnel and the ability to record data from each chamber under test. Concurrently, the muon beam is used to simulate the signal component of the experiment. Detectors such as RPCs, CSCs, DTs, GEMs and other gaseous detectors from various CERN experiments are tested here to confirm their functionality under these challenging conditions.

The experimental setup includes carefully placed iRPC prototypes, such as the the one used this study, positioned between two scintillators. In addition to the muon beam, a Cs-137 gamma source simulates nearly three times the high background rate expected during the Phase II upgrade of the LHC, which will be around 2 kHz/cm^2. This gamma source is strategically placed a few meters from the detectors, at the center of the bunker.

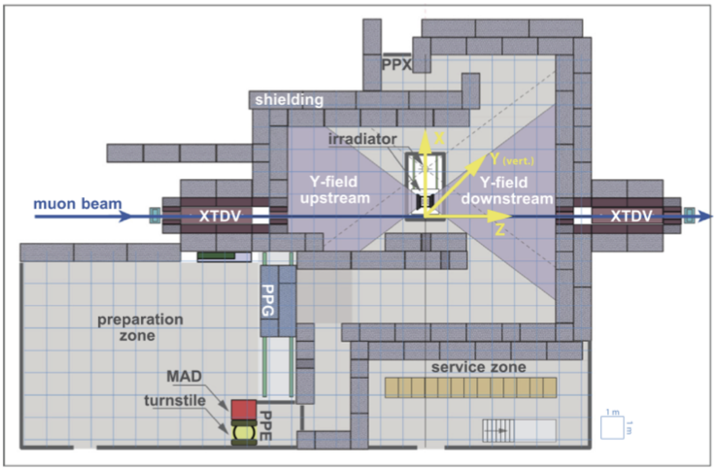

Figure 7: Floor plan of the Gamma Irradiation Facility GIF++. CMS-RPC chambers are strategically positioned in the upstream area. The high voltage supply and signal readout mainframe are situated on the first floor of the service zone, while the gas mixer is located on the second floor of the service zone [5]

There are currently two operational modes for the muon beam: one with the beam ON and with the beam OFF. The availability of these modes largely depends on the operations and maintenance conducted by the staff at the SPS accelerator, where the muon beam is generated. Regardless of the beam's status, testing can proceed using the radioactive source and a set of adjustable filters and the chamber position to control the amount of radiation received by the detectors.

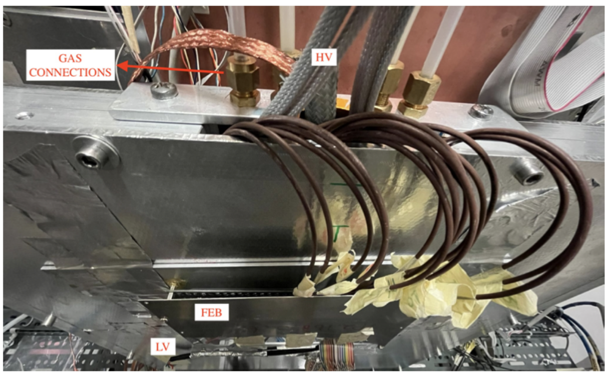

Figure 8: Chamber prototype placed in the upstream area of GIF++ bunker. The chamber has high voltage connections (HV), low voltage (LV) to power the Front-End board and gas connections for the gaps (supply and return for each gap [6].

As illustrated in Figure 7, the bunker is divided into two zones, with the upstream area designated for the placement of iRPCs. In this configuration, the detectors situated in the upstream zones are equipped with a set of absorption (ABS) filters, which can be independently adjusted to facilitate different experimental setups.

All iRPC studies were conducted in the upstream zone with the gamma source both ON and OFF, utilizing ABS filters with values of 1, 2.2, 3.3, 4.6, 6.9, 10, and 22. Each filter value corresponds to a specific background radiation rate depending of the chamber distance from the source. For the chamber used in this analysis, it was approximately 2, 1, 0.8, 0.6, 0.4, 0.3, and 0.1 kHz/cm^2, respectively.

The relationship between the ABS value and the radiation level is inversely proportional: the lower the ABS value, the higher the radiation reaching the detector. Consequently, there is a proportional relationship between the background rate and the amount of radiation. In these tests, the highest background rate observed was 2.2 kHz/cm^2 with the 1 ABS filter, which is nearly three times the anticipated background rate for the HL-LHC.

For this study, an iRPC chamber prototype was used, as shown in Figure 8, made of double 1.4 mm gap with an area of 50 x 50 cm^2. Due to the lack of final iRPC electronics, it was used an electronics prototype from KODEL laboratory, in KOREA, with a charge threshold of 60 fC. The strips were design as the existing RPCs, with single strip readout by the electronics.

In early 2023, the KODEL-E chamber was installed at GIF++ to conduct measurements with different CO_2-based gas mixtures. The primary objective of these experiments was to evaluate the chamber's performance under varying environmental conditions and to optimize the gas mixture for maximum efficiency. The tests focused on assessing the chamber's efficiency, time resolution, and rate capability when exposed to high radiation levels.

A key component of this system was the Front-end Board (FEB), also customized by KODEL. The FEB was designed to operate in current-sensitive mode for input signals, featuring an input impedance of 20 Ω, an amplification gain of 200, and a Low-Voltage Differential Signaling (LVDS) pulse width of 60 ns, with a threshold of 0.5 mV, corresponding to approximately 60 fC.

To ensure reliable operation and data collection from the detector, a Web-based Detector Control System (WebDCS) was implemented. This system provided real-time monitoring and control of critical parameters such as voltage, current, and environmental conditions like temperature and humidity. By leveraging the WebDCS, the detector's performance could be optimized and monitored remotely, allowing adjustments to be made swiftly during testing and operation. Such a system is indispensable, particularly in high-radiation environments like the GIF++.

The results from these tests will be analyzed in this report to assess the performance and viability of the iRPC chambers with different CO_2-based gas mixtures.

5 Data analysis

To conduct the analysis using data taken from the GIF++ facility, we employed the PyROOT framework. This framework allows us to read ROOT files generated by GIF++ and extract the necessary data for studying muon reconstruction efficiency. PyROOT facilitates the efficient handling of ROOT data, enabling us to perform detailed analyses and draw meaningful conclusions from the experimental results.

In this section, we will briefly discuss each of these characteristics for the KODEL-E chamber and describe the steps applied to obtain all of these results. As a starting point for the offline reconstruction analysis, we first need to examine what a raw event looks like and explore the ROOT files generated, as shown in Figure 9.

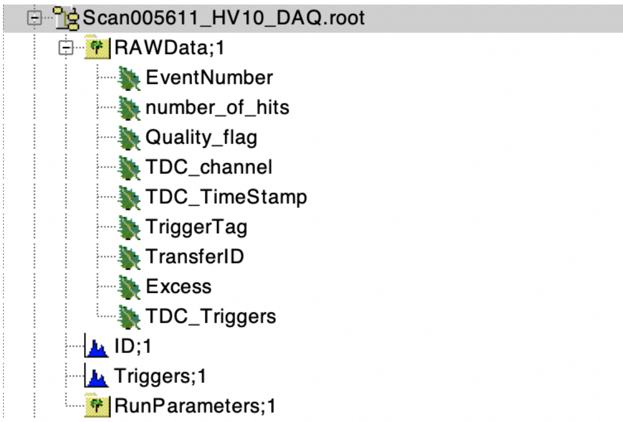

Figure 9: Screenshot of the ROOT browser showing the content of one of the scans taken from the GIF++, including data like the TDC channel data, event numbers, and other relevant information for the analysis.

For each type of scan, a specific number is assigned, which corresponds to a particular source and gas used in the detector. For instance, in Figure 9, we see the scan number 00005611. In the GIF++ notation, a scan number with four non-zero digits signifies that normal gas was used, whereas a scan number with only three non-zero digits indicates the use of eco-gas webdcs.

All ROOT files generated will contain the same structure of trees, leaves, and histograms. Within the `RAWData` section, information such as the TDC (Time Digital Converter) channel, number of hits, and other parameters are recorded. These parameters are crucial for the analysis, which will be detailed in the following sections.

5.1 Clusterization algorithm

Once an iRPC starts collecting data, a raw digital event is represented as a collection of fired Time Digital Converter (TDC) channels. When these TDC channels are plotted against time, they provide a schematic view of the signals detected by each strip within a specific time window, since each TDC channel corresponds to a strip signal.

To identify each possible time window, one should first plot the total number of hits versus time. This plot helps distinguish hits that occur inside or outside the "muon spill" period. The term ”muon spill” refers to a specific period or event when a muon beam passes into the detector.

From Figure 10, which shows the data collected outside the muon spill, we can observe the baseline noise and background hits that are present when the muon beam is not active. This period is crucial for understanding the noise of the chamber.

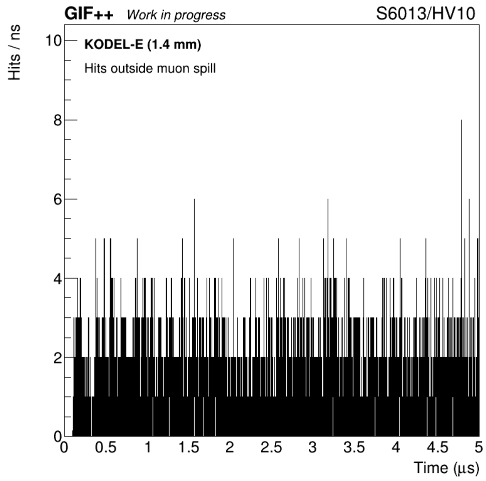

Figure 10: Time profile for events outside the muon spill.

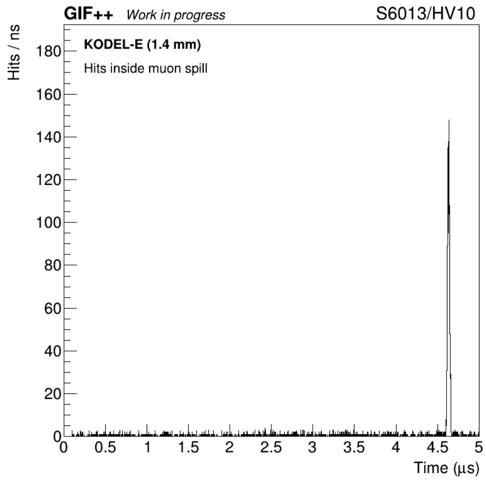

Figure 11: Time profile for events with the muon beam ON.

In this plot, the histogram on Figure 10 of hits versus time reveals the random fluctuations and constant noise activity that occurs independently of the muon beam. By analyzing these data, we can estimate the noise rate and compare the data from Figure 11 with the data obtained during the muon spill this allows us to differentiate between signal and noise more effectively. The muon spill data typically show as a clear peak in the number of hits during the injection period.

To conduct a more detailed analysis, we can focus specifically on this time range by ”zooming in.” By narrowing our scope to this interval, we can perform a fit on this data will allow us to extract key parameters, such as the muon time window, which will be crucial for generating efficiency plots in subsequent analyses.

Using a Gaussian fit in the data allows us to extract key properties such as the peak mean and peak width. The peak mean represents the most probable time at which the muon signal is detected, while the peak width provides information about the time resolution of the detector. A narrower peak width indicates better time resolution, which is critical for accurate particle track reconstruction.

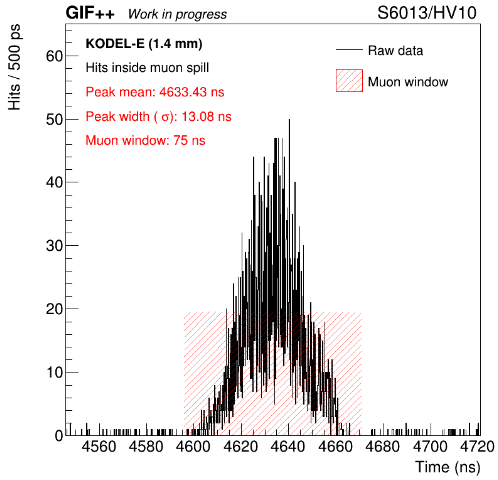

Figure 12: Time profile inside the muon spill with a zoom in the range of 4,5 to 4,75 μs.

Using the information on the muon peak width, we can define the muon time window, typically set as three times the peak width. This time window is essential for accurately capturing muon signals while filtering out irrelevant events. However, when the radiation sources are turned ON, gamma hits can also occur within this muon time window. These gamma hits introduce background noise and can lead to false positives, thereby inflating the measured efficiency.

To mitigate this issue, correction methods are necessary to account for the gamma hit contributions. One effective approach is to reduce the muon time window to a fixed value of approximately 75 nanoseconds. This value is chosen because, under source OFF conditions, the time window is predominantly around 75 nanoseconds.

By applying this fixed time window consistently across all analyses, the impact of gamma hits is minimized, ensuring that the efficiency measurements more accurately reflect true muon detections. This adjustment results in more reliable data and a clearer understanding of the detector's performance.

5.2 Efficiency curve

Following the results from the clusterization algorithm, an efficiency curve is constructed for the different sets of high voltages and the efficiencies recorded for the reconstructed muons within the iRPC detector. To determine the efficiency, we must consider two scenarios: one with the source OFF (no gamma radiation impinging on the detector) and another with the source ON (gamma radiation present).

For the first scenario, where the source is OFF, the muon reconstruction efficiency is calculated as the ratio of the number of muons clusters reconstructed by the iRPC to the number of events recorded by the trigger system (the array of scintillators), both measured within the muon time window. This can be expressed mathematically as:

$$\epsilon = \frac{N_{clusters}}{N_{Trigger}} \tag{1}$$

As discussed previously, the presence of a radioactive source during measurements significantly affects muon event reconstruction by introducing background signals from particles emitted by the source impinging on the detector. Therefore, it is essential to correct the raw efficiency.

This additional effect is illustrated in Figure 10, where gamma particles produce a constant number of hits in the time profile. To isolate the signal and account for the background contributions, we use Bayesian probability theory for efficiency correction.

Given that the background is present even within the muon time window, the total efficiency P_{tot} measured within this window includes both muon efficiency $P(\mu)$ and background efficiency P(bkg).

The background contribution can be calculated by measuring hits in a time interval outside the muon time window, of equal length to the muon window, and directly evaluating the background efficiency. Once these components are obtained, the Bayesian probability formula for non-independent measurements is used:

$$P(tot) = P(\mu) + P(bkg) - P(\mu)P(bkg) \tag{2}$$

so that the muon efficiency is corrected simply as:

$$P(\mu) = \frac{P(tot) - P(bkg)}{1 - P(bkg)} \tag{3}$$

Under these circumstances, P_{tot} represents the raw efficiency obtained without background correction, as described by Equation 1. This algorithm is applied to each HV point for each scan, resulting in a set of efficiencies for each high voltage setting. With this data, one can plot an efficiency curve for the recorded data.

The functional form of the efficiency data can be parameterized by a sigmoid function (S-curve), which considers three parameters: the maximum efficiency ϵ_{max} at the plateau (the highest value achieved when the detector reaches its maximum performance), the high voltage at 50% efficiency $HV_{50\%}$, and the parameter λ, which has dimensions of inverse voltage. The nominal model can be expressed as:

$$\epsilon = \frac{\epsilon_{\text{max}}}{1 + e^{-\lambda(\text{HV}_{\text{eff}} - \text{HV}_{50\%})}} \tag{4}$$

The data extraction and fitting process was conducted for each of the four gas mixtures tested. This task was accomplished using a Python script via the PyROOT function ‘Fit‘, which enabled us to input the three main parameters along with the dataset.

The function provides the optimized parameters after the fitting process, as well as the uncertainties in the form of a covariance matrix.

The working point (WP) is defined as the HV in the knee (HV where efficiency is 95%) plus 150 V. This point represents where the detector achieves 95% of its maximum efficiency in the absence of other contributions. Simply, we use the following formula:

$$\text{WP} = \text{HV}_{95\%} + 150\,\text{V} = \frac{\log 19}{\lambda} + \text{HV}_{50\%} + 150\,\text{V} \tag{5}$$

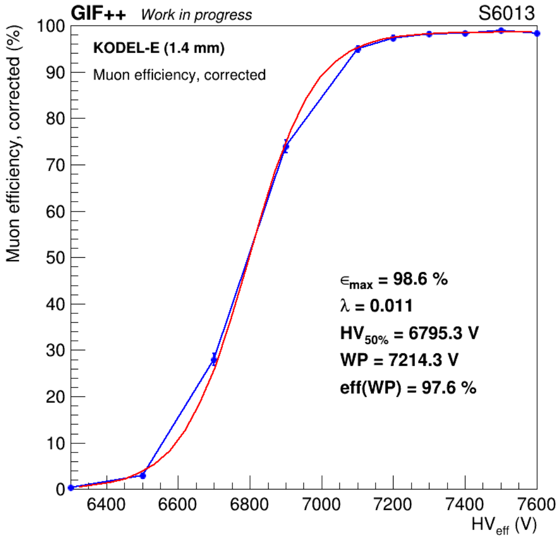

Figure 13: Efficiency plot for scan 6013.

At the end, the total minimized function is plotted along the experimental data and the calculated WP for each ABS filter. A normal efficiency curve for a single scan looks like the one in Figure 13. One important thing to notice is that without a plateau, the WP can not be appropriately defined.

Now we need to organize all the curves into a single plot to compare the performance of different gas mixtures with the same ABS values and the same mixtures with different ABS values. This comprehensive visualization will help analyze how each variable affects the efficiency and performance of the detector for different gaseous mixtures.

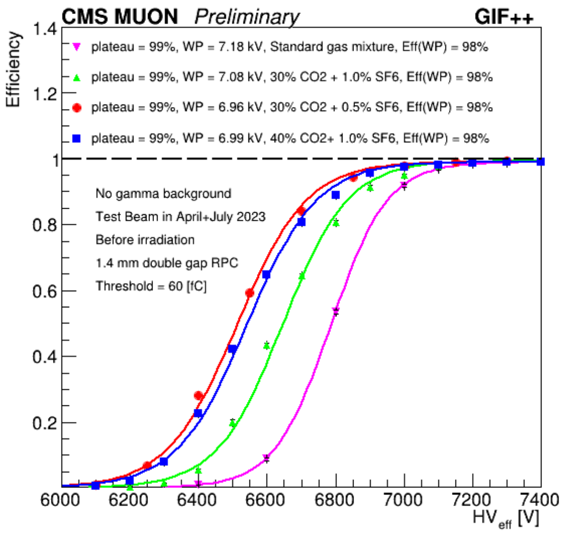

Figure 14: Efficiencies for different mixtures with source OFF for data taken in 2023.

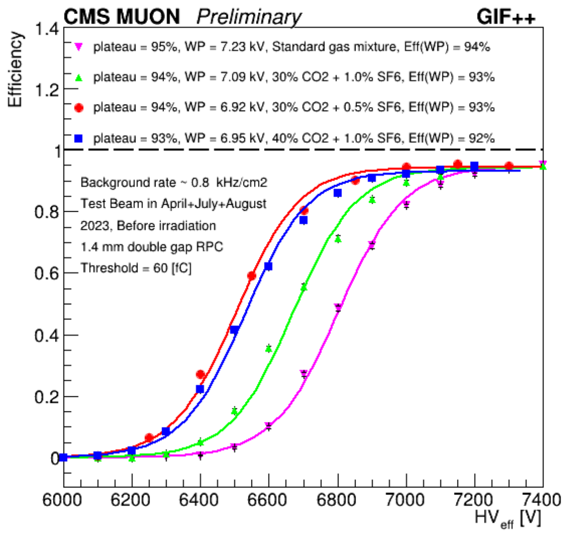

Figure 15: Efficiencies for different mixtures with ABS factor of 3.3 for data taken in 2023.

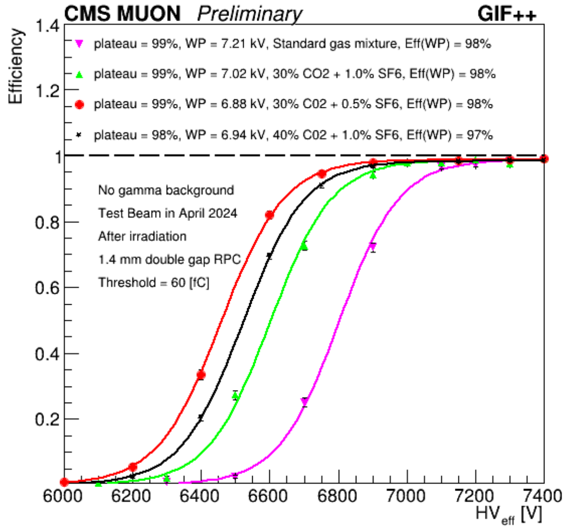

Figure 16: Efficiencies for different mixtures with source OFF for data taken in 2024.

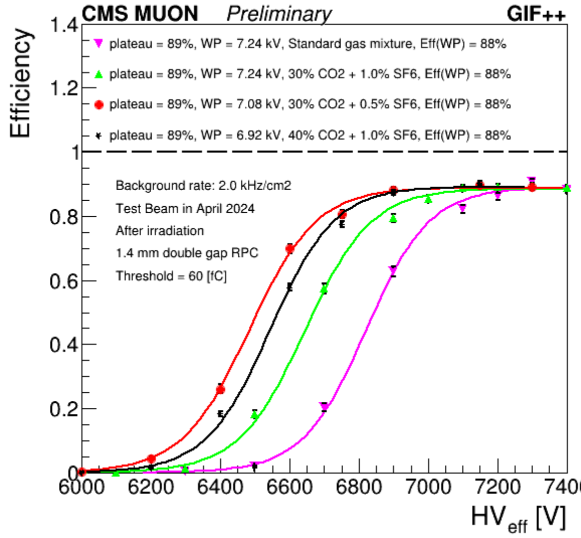

Figure 17: Efficiencies for different mixtures with ABS factor of 1 for data taken in 2024.

Between 2023 and 2024 data taking, a dedicated irradiation period was taken in order to accumulate charge with the chamber flushing the gas mixture with 30 % CO_2 and 1.0% SF_6. During the irradiation process, a total charge of 40 mC/cm^2 was integrated, corresponding to approximately 4% of the expected charge for the HL-LHC, with a safety factor of 3 (1 C/cm^2).

In Figures 14, 15, 16, and 17, we observe the efficiency of different gas mixtures listed in Table 2, with the source OFF and ON and different periods (before and after dedicated irradiation campaign). This comparison allows us to analyze how each mixture performs under identical conditions, specifically examining the impact of varying gas compositions on detector efficiency in the absence, presence and different gamma background rates.

By studying the efficiency curves, we can assess the influence of each gas mixture on detector performance, particularly the efficiency of muon detection and the overall signal-to-noise ratio. This analysis is crucial for optimizing the gas mixture to achieve the best possible detector performance.

In these mixtures, $C_2H_2F_4$ plays key roles in the ionization process and subsequent particle shower, SF_6 controls the avalanche process within the detector. CO_2 acts as a moderating gas, influencing primary ionization as muons pass through the detector. It helps regulate the energy and speed of free electrons, thereby managing the initial ionization and overall gain of the detector. However, increasing the concentration of CO_2 tends to lower the Working Point (WP), as it reduces the density of the gas.

Conversely, SF_6 serves as a quenching agent, essential for controlling the electron avalanche that follows primary ionization. With its high electron affinity, SF_6 captures free electrons during the avalanche, preventing uncontrolled growth of the electron shower. This control is critical for maintaining detector stability and precision, especially in high-radiation environments. Increasing the concentration of SF_6 tends to raise the WP, as it enhances avalanche control, allowing the detector to operate more efficiently under intense radiation conditions.

When the source is OFF, we evaluate the baseline efficiency of the detector, providing insight into the inherent performance of each gas mixture without external interference. The roles of CO_2 as a moderator and SF_6 as a quencher ensure the detector operates at nearly maximum efficiency under these conditions.

There was no drop in efficiency for Source OFF comparing different gas mixtures (Figure 14). The different drop in efficiency under high gamma background conditions highlights the importance of optimizing the gas mixture, particularly by adjusting CO_2 and SF_6 concentrations, to minimize background radiation impact. Increasing too much the percentage of CO_2 will decrease the cross section with $C_2H_2F_4$, degrading efficiency due to lower probability of the muon to interact.

When the source is ON, particularly under the highest gamma background (source 1), efficiency drops higher is the amount of CO_2. This decrease reflects the gas response to increased gamma radiation. High gamma backgrounds can also cause gamma hits to overlap with muon signals, degrading detection accuracy and reducing overall efficiency. Since FEB dead time is around 80 ns, overall efficiency drop is expect, by 1% further drop with 30% of CO_2 and 2% with 40% of CO_2, as shown in Figure 15.

After irradiation, we have still same performance for Source OFF, but same drop in efficiency observed (88%) for all gas mixtures tested (Figures 16 and 17). This analysis is still ongoing, but since the drops are the same observed, we believe it's due to electronics issue, since the adapted KODEL FEB is not designed to operate with the extreme conditions imposed by this radiation level.

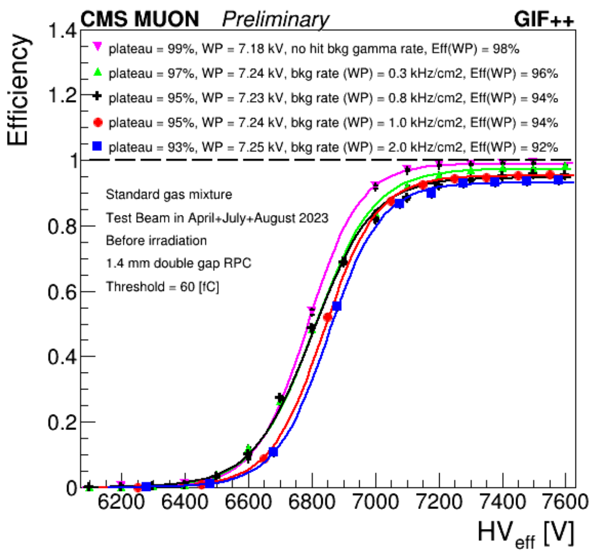

Figure 18: Efficiency for the standard gas mixture with sources: OFF, 10, 3.3, 2.2, 1 for the 2023 data taking.

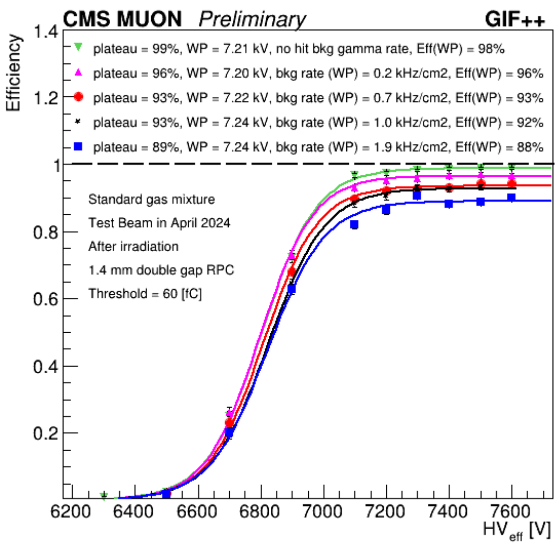

Figure 19: Efficiency for the standard gas mixture with sources: OFF, 10, 3.3, 2.2, 1 for the 2024 data taking.

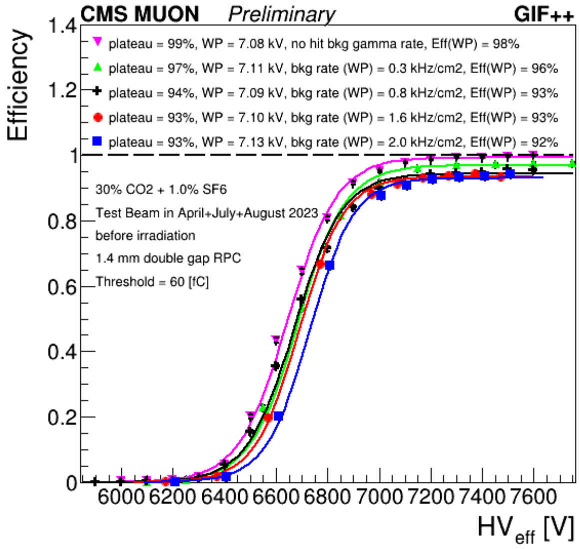

Figure 20: Efficiency for the 30% CO_2 + 1.0% SF_6 mixture with sources: OFF, 10, 3.3, 2.2, 1 for the 2023 data taking.

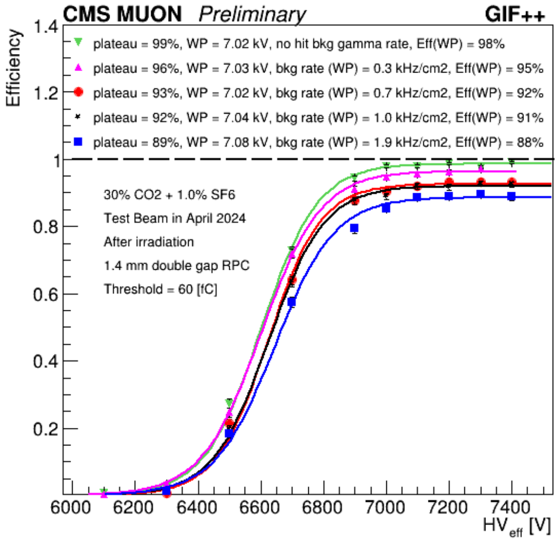

Figure 21: Efficiency for the 30% CO_2 + 1.0% SF_6 mixture with sources: OFF, 10, 3.3, 2.2, 1 for the 2024 data taking.

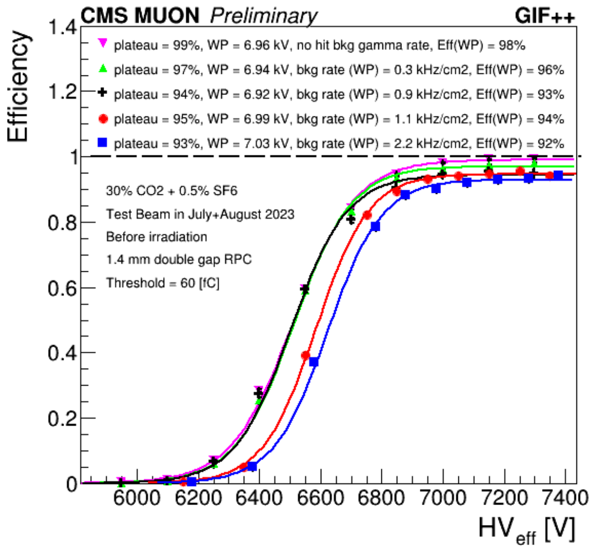

Figure 22: Efficiency for the 30% CO_2 + 0.5% SF_6 mixture with sources: OFF, 10, 3.3, 2.2, 1 for the 2023 data taking.

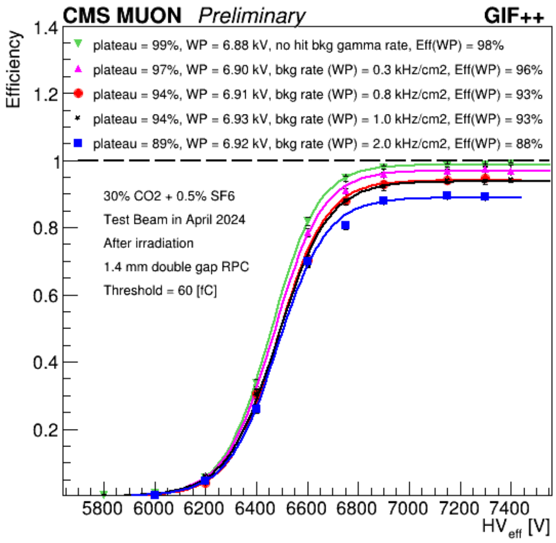

Figure 23: Efficiency for the 30% CO_2 + 0.5% SF_6 mixture with sources: OFF, 10, 3.3, 2.2, 1 for the 2024 data taking.

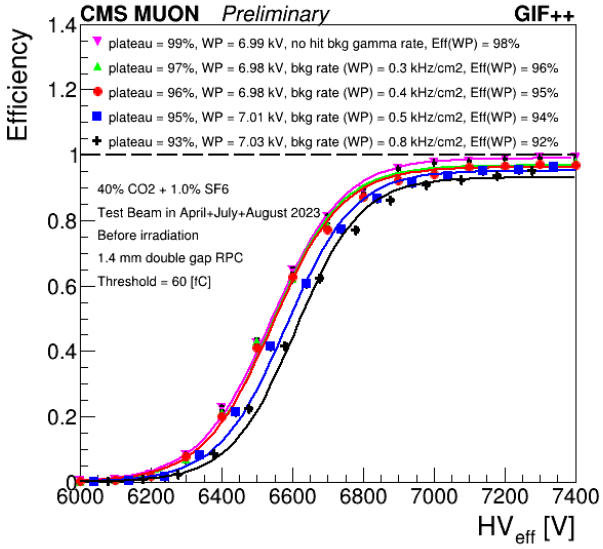

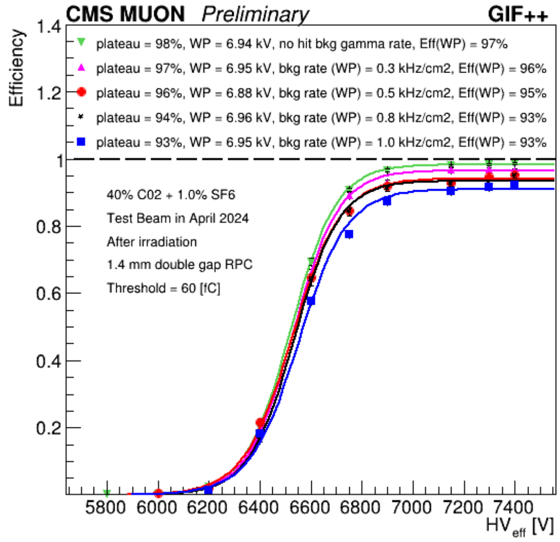

Figure 24: Efficiency for the 40% CO_2 + 1.0% SF_6 mixture with sources: OFF, 10, 6.9, 4.6, 3.3 for the 2023 data taking.

Figure 25: Efficiency for the 40% CO_2 + 1.0% SF_6 mixture with sources: OFF, 10, 6.9, 3.3, 2.2 for the 2024 data taking.

In Figures 18 to 25, we can observe the overall efficiency for the same gas mixtures under different ABS levels, presented in the following order: OFF, 22, 10, 6.9, 4.6, 3.3, 2.2, 1. We can compare and confirm the efficiency behaviour for different gas mixtures tested before and after irradiation. As it's clear the role of increasing CO_2 in the efficiency drop, the different amounts of SF_6 seems to play the same role. Given the high GWP of SF_6, the gas mixture with 30% of CO_2 and 0.5 % SF_6 seems promising. On the other hand, the irradiation effects are still under investigation.

These findings indicate that while the gas mixtures generally perform comparably, the impact of radiation exposure leads to diminished efficiency, highlighting the need for further investigation into the long-term behavior of these detectors under high-radiation environments.

6 Conclusion

In conclusion, this study provides a comprehensive evaluation of the efficiency of different gas mixtures used in iRPCs under various background radiation conditions. By systematically analyzing the performance of these detectors across different ABS levels and comparing various gas mixtures, we gain valuable insights into their operational characteristics and limitations.

The results show that, under ideal conditions with the source OFF, the detector achieves optimal efficiency with all tested gas mixtures. However, as the ABS level increases, particularly under high gamma background conditions, there is a small decrease in efficiency with the addition of CO_2. This highlights the detector's sensitivity to background noise and the challenges it faces in maintaining performance amidst increased radiation levels.

The efficiency plots for different gas mixtures and ABS levels reveal how each mixture influences the detector's ability to accurately detect muons while minimizing the impact of background noise. Specifically, the study demonstrates that gas mixtures can significantly affect the detector's performance, with some mixtures proving more effective in maintaining high efficiency despite increased background radiation. Notably, the mixture of 30% CO_2 and 0.5% SF_6 emerged as the best performer in terms of efficiency and lesser GWP.

By analyzing the data and refining the muon detection process, we can better understand the trade-offs between detector efficiency and background noise. This understanding is crucial for optimizing gas mixtures and improving detector performance in practical applications. Future work will focus on continuing to integrate charge and gather more data at the GIF++ facility to investigate potential aging effects in the chambers. This ongoing research is essential for ensuring reliable and accurate muon detection across a range of operating conditions.

References

[1] L. A. Cabrera, "Status and performance of the cms muon system in run2," p. 733, 02 2017.

[2] M. Gamal Ahmed Mohamed, "CMS iRPC assembly and Quality Control," 2023.

[3] K. Shchablo, *Development of fast timing detector for CMS experiment upgrade at CERN*. Theses, Université de Lyon, Dec. 2020.

[4] E. Voevodina and Fagot, "Re3/1 amp; re4/1 rpc chambers integration in the inner region of the forward muon spectrometer in the cms experiment," *Journal of Instrumentation*, vol. 14, p. C10027–C10027, Oct. 2019.

[5] D. Pfeiffer, G. Gorine, H. Reithler, B. Biskup, A. Day, A. Fabich, J. Germa, R. Guida, M. Jaekel, and F. Ravotti, "The radiation field in the gamma irradiation facility gif++ at cern," *Nuclear Instruments and Methods in Physics Research Section A: Accelerators, Spectrometers, Detectors and Associated Equipment*, vol. 866, pp. 91–103, 2017.

[6] J. P. Gomes Pinheiro, M. A. Shah, and L. Eiriz Sanchez, "Performance of new CO2 based mixture in CMS Improved Resistive Plate Chambers in HL-LHC environment," tech. rep., CERN, Geneva, 2024.

[7] N. Tepec Tinoco, "New eco-friendly gas mixture for Resistive Plate Chambers in CMS in the framework of HL-LHC," 2023.

[8] S. Chatrchyan, "Observation of a new boson at a mass of 125 gev with the cms experiment at the lhc," *Physics Letters B*, vol. 716, p. 30–61, Sept. 2012.

[9] G. Aad and Abajyan, "Observation of a new particle in the search for the standard model higgs boson with the atlas detector at the lhc," *Physics Letters B*, vol. 716, p. 1–29, Sept. 2012.

[10] G. Apollinari, I. Béjar Alonso, O. Brüning, M. Lamont, and L. Rossi, *High-Luminosity Large Hadron Collider (HL-LHC): Preliminary Design Report*. CERN Yellow Reports: Monographs, Geneva: CERN, 2015.

[11] T. Hebbeker and A. Korytov, "The Phase-2 Upgrade of the CMS Muon Detectors," 9 2017.

[12] CERN, "Cern publishes its first f-gas policy," 2023. [Accessed: 28-Sep-2024].

[13] E. Commission, "A european green deal," 2024. [Accessed: 28-Sep-2024].

[14] M. Abbrescia, V. Peskov, and P. Fonte, *Resistive gaseous detectors: designs, performance, and perspectives.* John Wiley & Sons, 2018.

[15] T. R. E. collaboration, :, L. Quaglia, M. Abbrescia, G. Aielli, R. Aly, M. C. Arena, M. Barroso, L. Benussi, S. Bianco, D. Boscherini, F. Bordon, A. Bruni, S. Buontempo, M. Busato, P. Camarri, R. Cardarelli, L. Congedo, D. D. J. Damiao, M. D. Serio, A. D. Ciaccio, L. D. Stante, P. Dupieux, J. Eysermans, A. Ferretti, G. Galati, M. Gagliardi, S. Garetti, R. Guida, G. Iaselli, B. Joly, S. A. Juks, K. S. Lee, B. Liberti, D. L. Ramirez, B. Mandelli, S. P. Manen, L. Massa, A. Pastore, E. Pastori, D. Piccolo, L. Pizzimento, A. Polini, G. Proto, G. Pugliese, D. Ramos, G. Rigoletti, A. Rocchi, M. Romano, A. Samalan, P. Salvini, R. Santonico, G. Saviano, M. Sessa, S. Simone, L. Terlizzi, M. Tytgat, E. Vercellin, M. Verzeroli, and N. Zaganidis, "Exploring eco-friendly gas mixtures for resistive plate chambers: A comprehensive study on performance and aging," 2024.

[16] E. "Ballabene and et al., "Performance of ATLAS RPC detectors and L1 Muon Barrel Trigger with a new CO_2-based gas mixture," 2024.